Extracting stellar emissivity via a machine learning analysis of MSX and LAMOST catalog data

Chuanxin Zhang,[1,*] Tianjiao Li,[2] Peng Jin,[1] Yuan Yuan,[3] Xiaoping Ouyang,[4] Fabio Marchesoni,[5,6] and Jiping Huang[1,†]

[1]*Department of Physics, State Key Laboratory of Surface Physics, and Key Laboratory of Micro and Nano Photonic Structures (MOE), Fudan University, Shanghai 200438, China*
[2]*MIIT Key Laboratory of Thermal Control of Electronic Equipment, School of Energy and Power Engineering, Nanjing University of Science and Technology, Nanjing 210094, China*
[3]*School of Energy Science and Engineering, Harbin Institute of Technology, Harbin 150001, China*
[4]*School of Materials Science and Engineering, Xiangtan University, Xiangtan 411105, China*
[5]*School of Physics Science and Engineering, Tongji University, Shanghai 200092, China*
[6]*Department of Physics, University of Camerino, 62032 Camerino, Italy*

(Received 24 October 2022; accepted 12 December 2022; published 30 December 2022)

Many astronomical studies model stars like radiating blackbodies with unit emissivity. Their conclusions should be reconsidered if the stellar spectral emissivity, ε_λ, were to be proven to be appreciably smaller. However, determining ε_λ from raw observational data poses serious technical challenges. Here, using a machine learning technique, we implemented an inverse model for calculating the stellar spectral radiation flux in a given spectral band emissivity. Radiation flux data in some spectral bands serve as input to determine the unknown model parameters. To this purpose, we chose 411 stars (361 from the Midcourse Space Experiment (MSX) catalog and 50 from the Large Sky Area Multi-Object Fiber Spectroscopic Telescope (LAMOST) catalog) as training samples of a stochastic particle swarm optimization algorithm. The mean values of the emissivity estimates thus obtained deviate significantly from the ideal blackbody value. Knowledge of the model parameters then enabled us to calculate the radiation fluxes in other spectral bands to compare with the existing observational data and thus validate our approach. Finally, based on the trained algorithm, we discuss our predictions for spectral bands where astronomical data are unavailable. Besides providing direct evidence against modeling stars as emitting blackbodies, our conclusions also call for more direct investigations of the stellar emissivity.

DOI: 10.1103/PhysRevD.106.123035

I. INTRODUCTION

Determining the star age is key to understanding the origin of the Universe [1]. The first step to determining it is to classify the observed star based on its spectral characteristics, say, whether it is a blue dwarf with an abnormally strong internal nuclear fusion reaction or a yellow dwarf with a moderate reaction intensity or, perhaps, an orange or red dwarf with a low reaction intensity [2]. Moreover, the spectral analysis of the radiation from the star can reveal valuable information about its effective temperature, atmosphere, ionization state, surface gravity, rotation rate, and the abundance of elements [3]. In this regard, we remind the reader that the wide spectral range of the James Webb Space Telescope, spanning from visible to near-(0.6–5.3 μm) and midinfrared (5–28 μm) [4–7], was specifically designed to allow high-precision measurements of star ages. A related observable essential in the study of stellar evolution is the radiation flux, which depends on the star luminosity and its distance from the Earth [8–12]. The observation of radiation fluxes in different spectral emission bands [13] provides additional information about celestial bodies.

One can estimate the radiation flux from a star by using models for the stellar effective temperature, band emissivity, and the detection angular parameter [14,15]. Stellar emissivity is the ratio of the radiation emitted by a star surface to the radiation emitted by a blackbody at the same wavelength. Thus, it ranges from 0 to 1 [16–20]. In fact, stars are not perfect blackbodies, and their emissivity is not the same across the entire emission spectrum [21–25]. The radiation fluxes measured by a detector may not conform to Planck's law predictions because of the wavelength

*cxzhang@fudan.edu.cn
†jphuang@fudan.edu.cn

dependence of the stellar emission and/or absorption processes [26]. Most of such processes takes place in the star atmosphere, which, in turn, is characterized by variable patterns of temperature, pressure, density, and element abundance [27]. Consequently, the relevant radiation flux cannot be accurately estimated if the star emissivity is conventionally set to 1 [28,29]. Indeed, the emissivity of a star should be evaluated together with its effective temperature to mitigate systematic errors in the estimates of the radiation fluxes [30,31]. On the other hand, determining the stellar spectral emissivity from raw observational data proved to be a challenging task, hence the often unwarranted assumption of stars as blackbody emitters.

The stellar effective temperature is a relatively well-investigated parameter due to its significance in the current theories of stellar evolution. One can estimate it by having recourse to different methods, namely, the direct measurement method [32–35], the infrared flux method [36–39], and the template matching method [40–42].

Contrary to the stellar effective temperature, there is no well-established method to extract reliable estimates of the stellar spectral emissivity from the available observational data. On the other hand, as anticipated above, assuming ideal emissivity $\varepsilon_\lambda = 1$ at all wavelengths may lead to unwanted inaccuracies in the determination of the radiation fluxes.

To address this problem, we propose a machine learning technique to train an inverse model for the radiation flux of a star of assigned spectral emissivity and effective temperature, i.e., with atmosphere thick enough for its surface to be in thermodynamic equilibrium [43]. In a previous study [44], a similar technique was applied to investigate the much simpler problem of the total radiation flux dependence on the effective temperature, alone. We implement a stochastic particle swarm optimization algorithm to determine the model parameters (spectral emissivity, effective temperatures, and detection angular parameters) in select spectral bands for a number of reference stars. The resulting mean emissivity values are confirmed to deviate significantly from the ideal blackbody value. After training, the model can be successfully employed to predict the radiation fluxes in other spectral bands and compare them with the existing observational data when available.

II. METHODS

A. Model of stellar radiation fluxes

Stellar radiation fluxes are usually extracted from the survey data of astronomical telescopes within specified spectral bands. The fluxes from a star detected on Earth may depend on many factors, including its temperature, the interstellar dust, and the star-detector distance. To simplify data analysis, we assume, as customary in the literature, stellar radiation fluxes to be a heuristic function of three effective stellar parameters only: namely, the band emissivity, the surface temperature, and the detection angular parameter. Sufficiently accurate knowledge of these three quantities yields reliable estimates of the relevant stellar radiation fluxes.

The spectral radiation flux in the wavelength band $(\lambda_i,\ \lambda_i + \Delta\lambda_i)$ from a blackbody at temperature T is described by Planck's law [45]

$$E_{b\lambda_i} = \int_{\lambda_i}^{\lambda_i+\Delta\lambda_i} \frac{c_1\lambda^{-5}}{\exp[c_2/(\lambda T)] - 1} \mathrm{d}\lambda, \tag{1}$$

where c_1 and c_2 are the first and second radiation constants, respectively. The corresponding band radiation flux from a star can be expressed as $E_{\lambda_i} = \varepsilon_{\lambda_i} E_{b\lambda_i}$, where ε_{λ_i} is the relevant star band emissivity. Recalling that the band radiation intensity is $I_{\lambda_i} = E_{\lambda_i}/\pi$ and the stellar detection solid angle is $\mathrm{d}\Omega = \pi r^2/R^2$ (see Fig. 1), then, the band radiation flux on the detector can be rewritten as $E_{p\lambda_i} = I_{\lambda_i}\mathrm{d}\Omega$; that is

$$E_{p\lambda_i} = \varepsilon_{\lambda_i}\xi \int_{\lambda_i}^{\lambda_i+\Delta\lambda_i} \frac{c_1\lambda^{-5}}{\exp[c_2/(\lambda T)] - 1} \mathrm{d}\lambda, \tag{2}$$

where r is the stellar radius, R is the star-detector distance, and

$$\xi = r^2/R^2 \tag{3}$$

is the detection angular parameter.

In conclusion, $E_{p\lambda_i}$ is expressed as a relatively simple function of three parameters, the band emissivity ε_{λ_i}, the

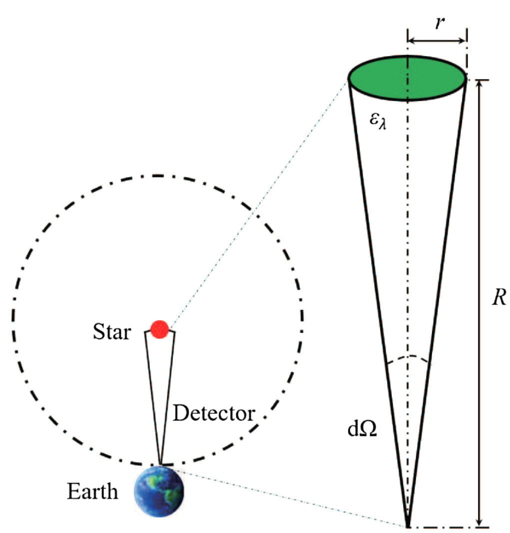

FIG. 1. The schematic diagram of the detection solid angle $\mathrm{d}\Omega$ of a star of emissivity ε_λ and radius r at a distance R from the observation point on Earth (not drawn to scale).

stellar effective temperature T, and the detection angular parameter ξ, i.e.,

$$E_{p\lambda_i} = f(\varepsilon_{\lambda_i}, T, \xi), \tag{4}$$

which defines the forward problem numerically addressed in this work.

B. Inverse problem

The difficulty of the problem is that the stellar radiation fluxes are known for several emission bands, but the model parameters, including the stellar effective temperature and band emissivity, are not. The model parameters need then to be extracted self-consistently from the known radiation fluxes. For this purpose, we developed a machine learning algorithm to solve the relevant inverse problem. The equations to solve can be formulated as

$$\varepsilon_{\lambda_i}, T, \xi = \mathcal{F}(E_{p\lambda_i}), \tag{5}$$

where the band index i runs from 1 to 3. We agreed to solve the inverse problem for the radiation fluxes in three specific wavelength bands of the Midcourse Space Experiment (MSX) catalog, namely, 6.8–10.8, 4.24–4.45, and 13.5–15.9 μm, respectively [46]. In the MSX catalog, infrared flux densities are reported for six wavelength bands between 4.22 and 25.1 μm [47]. Estimates of the right ascension, declination, and proper motion are also listed in the catalog. The flux densities of radio sources are defined as the emitted energy per unit frequency interval, unit area, and unit time interval [48–51]. The flux density unit adopted in the catalog is Jy [52], which can be converted to the corresponding SI unit as

$$1\ \mathrm{Jy} = 10^{-26}\ \mathrm{W/(m^2 \cdot Hz)}. \tag{6}$$

The radiation fluxes can be calculated by integrating the average energy density over the band [53], namely,

$$E_{\lambda_1-\lambda_2} = \int_{\lambda_1}^{\lambda_2} E_\lambda \mathrm{d}\lambda, \tag{7}$$

where E_λ denotes the radiation flux in the relevant wavelength interval or band.

For the three-band inverse problem, there are five unknown variables (stellar effective temperature, detection angular parameter, and three values of band emissivity), so Eq. (5) admits infinite solutions.

To numerically attack the problem, each emission band was divided into about 100 intervals. The stellar emissivity was assumed to be not far from 1.00 because stellar spectra are known to not differ much from blackbody spectra [28,29]. Eventually, the most appropriate variability range for the stellar band emissivity was narrowed down to (0.90,1.00). The effective temperature and detection angular parameter were computed for different values of the star emissivity. The choice corresponding to the minimum value of an adaptive parameter (the best fitness) was taken as the optimal final choice.

The deviation ΔT_{eff} of the stellar effective temperatures reported in the literature $T_{\mathrm{eff}}^{\mathrm{ref}}$ from the values $T_{\mathrm{eff}}^{\mathrm{present}}$ estimated in this work is defined as

$$\Delta T_{\mathrm{eff}} = T_{\mathrm{eff}}^{\mathrm{ref}} - T_{\mathrm{eff}}^{\mathrm{present}}. \tag{8}$$

The radiation fluxes corresponding to different detection bands are then calculated by using the estimated values of the band emissivity, stellar effective temperature, and detection angular parameter. Accordingly, the relative error δ associated with the calculated radiation fluxes is

$$\delta = (|E_c - E_m|/E_m) \times 100\%, \tag{9}$$

where E_c and E_m are, respectively, the radiation fluxes calculated through our technique and those reported in the telescope observational catalog.

C. Algorithm selection

The stochastic particle swarm optimization (SPSO) algorithm was designed to solve the inverse problem. The key idea is that the potential solutions are represented by particles moving in the solution space with a certain velocity. The optimal solution is determined by monitoring an adaptive parameter, the fitness, which quantifies how close the solution is to an objective value. The search space of D dimensionality is populated by M particles of coordinates $X_i = (x_{i1}, x_{i2}, \ldots, x_{iD})$, and velocity is populated by $V_i = (v_{i1}, v_{i2}, \ldots, v_{iD})$, with $i = 1, 2 \ldots M$. The best position experienced at a given time t by the ith particle is denoted by $P_i = (p_{i1}, p_{i2}, \ldots, p_{iD})$; the absolute best position among all M particles at the same time is $P_g = (p_{g1}, p_{g2}, \ldots, p_{gD})$.

The velocity V_i of each particle is given in terms of local and global values [54,55],

$$V_i(t+1) = wV_i(t) + c_1 r_1[P_i(t) - X_i(t)] + c_2 r_2[P_g(t) - X_i(t)]. \tag{10}$$

Here, t is the iteration time, w is the inertia weight, c_1 and c_2 are acceleration constants, and r_1 and r_2 are random numbers in the interval [0, 1]. Then, the new position X_i of the particle is determined by

$$X_i(t+1) = X_i(t) + V_i(t+1). \tag{11}$$

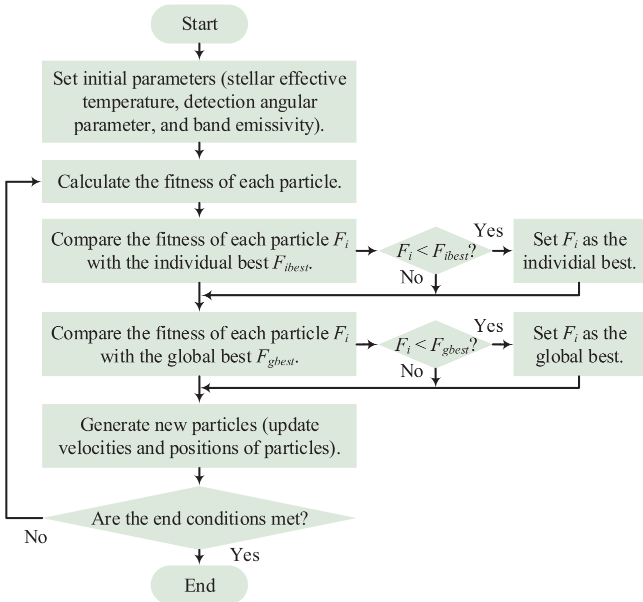

FIG. 2. The flow diagram of our SPSO algorithm.

In Fig. 2, we display the flow diagram of our SPSO algorithm. The steps for inverse computing the stellar parameters are as follows:

Step 1: Set the initial parameters of the system. The initial parameters include stellar effective temperatures, detection angular parameters, and band emissivity values.

Step 2: Calculate the fitness of each particle. The fitness value of the ith particle corresponds to its objective function value defined by

$$F_i = \sqrt{[(E_{ipa} - E_{ipb})/E_{ipa}]^2}, \tag{12}$$

where E_{ipa} represents the initial value of the inverse problem and E_{ipb} is the computational value of the particle.

Step 3: Compare the fitness F_i of the particle with its individual best $F_{i\mathrm{best}}$ at that time. If $F_i < F_{i\mathrm{best}}$, set this value as the current $F_{i\mathrm{best}}$, and record the corresponding particle position.

Step 4: Compare the fitness value of each particle F_i with the global best F_{gbest} at that time. If $F_i < F_{\mathrm{gbest}}$, set this value as the current F_{gbest}, and record the corresponding particle position.

Step 5: Generate the new particle and update the velocity and position of other particles using Eqs. (10) and (11). If $X_j(t) = P_j$ or $X_j(t) = P_g$, the position of the jth particle is generated randomly.

Step 6: Determine whether the end conditions are met. If the best fitness is less than the preset value or the iteration number reaches the preset maximum, then the process is terminated. Otherwise, increase the iteration index, $t = t + 1$, and go back to Step 2.

In our computations, we set the algorithm parameters as follows: number of particles $M = 50$; maximum number of iteration $t = 10,000$; inertia weigh $w = 0.0$; acceleration constants $c_1 = 1.80$ and $c_2 = 1.80$; and space dimensions equal the number of variables in the problem, $D = 3$. The expected solution ranges are 1000–20,000 K for the effective temperatures, 1.0×10^{-21}–1.0×10^{-16} for the detection angular parameters, and 0.90–1.00 for the band emissivity values. However, the above ranges have been expanded to meet the computing requirements, namely, $1.0 \times 10^{2.5}$–$1.0 \times 10^{4.5}$ K for the effective temperatures, 1.0×10^{-26}–1.0×10^{-10} for the detection angular parameter, and 0.90–1.00 for the band emissivity values. These latter ranges determine the boundaries of the particle swarm space.

D. Algorithm details

1. Effects of the number of particles on convergence

The number of particles M in the SPSO algorithm has a direct impact on the inversion efficiency and therefore on the output accuracy. Thus, one needs to determine an optimal choice for M. There are two algorithm "end" criteria: (1) the iteration accuracy is below a fixed level of 10^{-10}, and (2) the iteration number (or time) is larger than 10,000.

The convergence trends for different M values (10, 20, 50, 70, and 100) were compared to choose the optimal particle number. The best fitness values characterize the convergence trends as a function of the iteration time as shown in Fig. 3(a).

The best fitness decreases with the growth of iteration time until it hits the minimum value 1.37×10^{-8}. For $M = 10$, the convergence is the slowest. Convergence is reached after 1601 iterations for $M = 10$ and 501 for $M = 20$ and 301 for the remaining M values. The convergence trend is the most natural benchmark to choose the optimal value of M; however, the code running times should also be considered for practical purposes. Figure 3(b) shows the algorithm running times for $M = 10$, 20, 50, 70, and 100. All the calculations were performed on a 2.80 GHz Intel Core i7-7700HQ processor. The running time grows with increasing M, from 62 min for $M = 10$ to 636 min for $M = 100$.

In conclusion, when computing the model parameters, increasing M significantly increases the computation time without appreciably lowering the best fitness. Therefore, taking into account both factors, computation times and accuracy, we set $M = 50$ (for which the running time is 331 min).

2. Effects of the band emissivity on convergence

Figure 3(c) shows the best fitness as a function of iteration time with different band emissivity values, 0.90, 0.93, 0.95, 0.97, and 1.00.

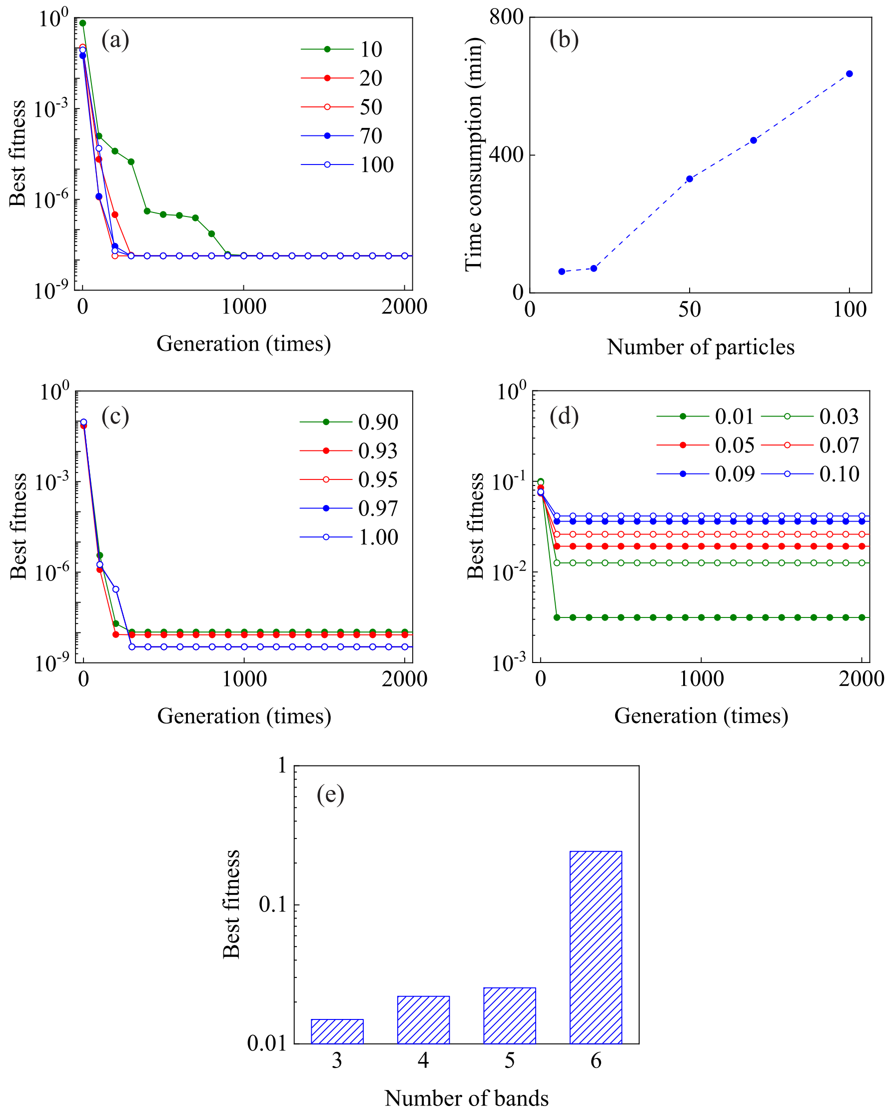

FIG. 3. (a) Best fitness vs iteration time with different numbers of particles, 10, 20, 50, 70, and 100. (b) Computing time to achieve convergence vs particle number. Best fitness minimum vs iteration time for (c) different emissivity values, 0.90, 0.93, 0.95, 0.97, and 1.00 and (d) randomized flux with σ [Eq. (14)], 0.01, 0.03, 0.05, 0.07, 0.09, and 0.10. (e) Best fitness minima for different numbers of input bands.

All the corresponding best fitness curves decay with the iteration time and reach their minimum after 301 iterations. In particular, the best fitness minima are 1.04×10^{-8} and 8.46×10^{-9} for emissivity equal, respectively, to 0.90 and 0.93 and 3.38×10^{-9} for all other emissivity values. In any case, the minimum value of the best fitness is no larger than 1.00×10^{-8} for an appropriately high number of iterations. This proves that our algorithm can be used to determine the inverse problem parameters in the full emissivity range considered in this work.

3. Effects of band flux uncertainties on convergence

To assess the stability of our inverse problem solution against the uncertainty of the input data, we generated random deviations to the catalog band-flux data [56]. The actual, Y_{exact}, and the modified values of the band flux, Y_{est}, have been related as

$$Y_{\mathrm{est}} = Y_{\mathrm{exact}} + \sigma \cdot \eta, \tag{13}$$

where η is a normally distributed random variable with mean value 0 and standard deviation 1. For a measured error γ at 99% confidence, the standard deviation σ of the measured flux is

$$\sigma = (Y_{\mathrm{exact}} \cdot \gamma\%)/2.576. \tag{14}$$

The relative error δ_{rel} of the estimated flux versus the exact one is

$$\delta_{\rm rel} = \frac{Y_{\rm est} - Y_{\rm exact}}{Y_{\rm exact}}. \quad (15)$$

We then calculated the radiation fluxes of bands 1–6. Figure 3(d) displays the best fitness as a function of the iteration time for the deviation σ, 0.01, 0.03, 0.05, 0.07, 0.09, and 0.10.

All best fitness curves decay with the iteration time and reach their minimum after 201 iterations. The exact values of best fitness minima are 0.0031, 0.0126, 0.0192, 0.0260, 0.0362, and 0.0414, respectively, for $\sigma = 0.01$, 0.03, 0.05, 0.07, 0.09, and 0.10. In any case, the minima of best fitness are low enough to ensure the stability of our numerical solutions even in the presence of uncertainties in the input band-flux data.

4. Effect of the band number on convergence

Figure 3(e) shows the best fitness minima versus the number of spectral bands used, namely, 0.015, 0.022, 0.025, and 0.242, respectively, for 3, 4, 5, and 6 bands. The lowest minimum of the best fitness was obtained by using data from three bands.

III. RESULTS

The spectral detection bands of Earth-based telescopes are limited. Radiation fluxes in additional bands are accessible through orbiting detectors, while observational data are still rather sparse for the remaining bands. Our inverse method is construed to fill this gap. The model parameters are inverse optimized based on the known radiation fluxes in certain accessible bands. After the key stellar parameters, namely, the effective temperature, detection angular parameters, and band emissivity, have been determined, the stellar radiation fluxes in all other bands can be predicted as solutions of the forward problem. In the present study, our main source of observational data was the MSX catalog [46]. The catalog organizes flux data for 177,860 stars into six detection bands, namely, bands 1–6 with wavelengths 6.8–10.8, 4.22–4.36, 4.24–4.45, 11.1–13.2, 13.5–15.9, and 18.2–25.1 μm, respectively.

Because of its nonlinear nature, the inverse problem can only be tackled numerically. Considering that the effective temperatures range between 1000 and 50,000 K, and the detection angular parameters span several orders of magnitude, a satisfactory solution would elude any standard numerical methods. For this reason, we had recourse to the SPSO algorithm, a variation of the popular particle swarm optimization algorithm, recently developed for better convergence [54,55].

A. Selection of number of inverse bands

The solution to the inverse problem requires observational data for an appropriate number of spectral bands. The relevant variables are the effective temperature, the detection angular parameter, and the emissivity. Moreover, the emissivity is a spectral function that yields distinct values for the different bands. Therefore, the number of unknowns is larger than the number of equations to solve. To circumvent this difficulty, we compared results from a variety of different input combinations, as reported below.

We ran our SPSO algorithm with initial effective temperature of 5000 K, detection angular parameter 2.0×10^{-19}, and emissivity 1.00. Figure 4(a) illustrates the convergence of the algorithm for different numbers of the bands available on the MSX catalog. The convergence quantifier adopted here is the best fitness parameter defined by Eq. (12). All curves on display quickly converge with increasing of the number of iterations. More remarkably, the minimum best fitness value is achieved for three bands. For this reason, we finally opted to numerically solve the inverse problem at hand by using the observational data from three spectral bands.

B. Selection of band combinations

The next question to address is how to select the most appropriate spectral bands for our analysis. As the MSX provides data for six bands and we only need three of them, we can choose from 20 combinations. Results from six band groups have been compared in detail for best algorithm performance, namely, group A (band 1, band 2, and band 3), group B (band 1, band 3, and band 5), group C (band 1, band 3, and band 6), group D (band 1, band 5, and band 6), broup E (band 2, band 3, and band 4), and group F (band 4, band 5, and band 6).

The algorithm was run for each band combination and different preset flux output errors. Figure 4(b) compares the solution's best fitness at increasing output errors for the six band groups. Group B exhibits the most stable value of the best fitness. The best fitness of group A is higher than group B for errors larger than 0.06, and so is the best fitness of group C but for errors smaller than 0.10. Finally, the best fitness of groups D, E, and F are all systematically larger than group B. Thus, group B (band 1, band 3, and band 5) was selected as our best choice for the SPSO solution of the inverse radiation flux problem.

C. Comparison of stellar effective temperature

Having tested the performance of our SPSO algorithms, we calculate now the stellar effective temperatures $T_{\rm eff}^{\rm present}$ and compare our results with the corresponding reference values $T_{\rm eff}^{\rm ref}$ reported in the literature [57–60].

The upper panel of Fig. 4(c) shows a comparison between $T_{\rm eff}^{\rm present}$ and $T_{\rm eff}^{\rm ref}$ for a sample of 90 stars, each represented by a blue circle [57–60]. The estimated effective temperatures span the relatively wide range 3500–6600 K. The representative points are concentrated around the solid black (diagonal) line, with most of them lying in the gray shaded area. This means that our relative

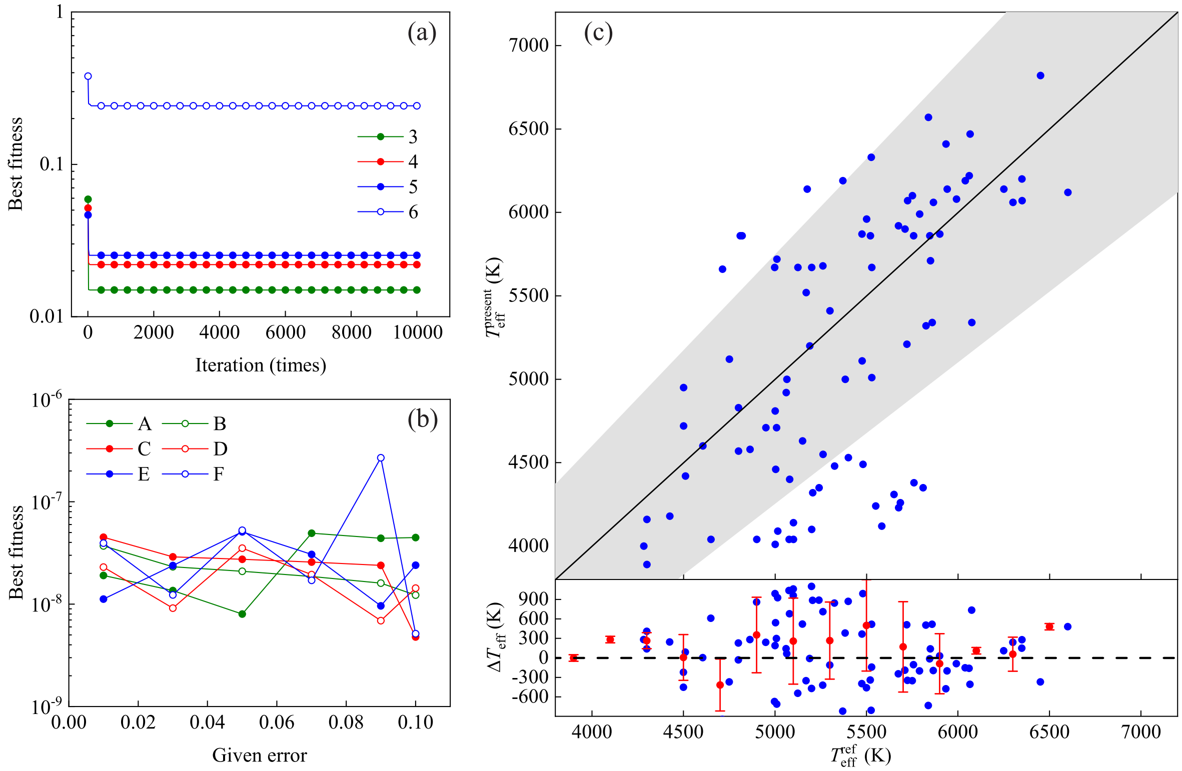

FIG. 4. (a) Best fitness vs iteration number for the SPSO algorithm operating on a different number of bands, 3, 4, 5, and 6. (b) Best fitness vs preassigned output error for the six band groups A–F. (c) Computed, $T_{\rm eff}^{\rm present}$, vs reported stellar effective temperatures, $T_{\rm eff}^{\rm ref}$ [57–60], for 90 stars (blue solid circles). Upper panel: the $(T_{\rm eff}^{\rm present}, T_{\rm eff}^{\rm ref})$ pair for each star; the black solid (diagonal) line represents the identity $T_{\rm eff}^{\rm present} = T_{\rm eff}^{\rm ref}$; circles falling inside the gray shaded area correspond to relative errors of the effective temperatures lower than 15%. Lower panel: the deviations $\Delta T_{\rm eff}$ are plotted vs $T_{\rm eff}^{\rm ref}$; see Eq. (8). Their mean values and standard deviations in $T_{\rm eff}^{\rm ref}$ bins of width 200 K (in the range 3500–6700 K) are indicated respectively by red points and bars. The dashed black (horizontal) line denotes the reference condition $\Delta T_{\rm eff} = 0$ K.

error on the effective temperatures of most stars is less than 15%; that is, the calculated temperatures are consistent with the existing data.

The deviations $\Delta T_{\rm eff}$ between reference, $T_{\rm eff}^{\rm ref}$, and estimated effective temperatures, $T_{\rm eff}^{\rm present}$ [see Eq. (8)], are reported in the lower panel in Fig. 4(c). The mean values and standard deviations of $\Delta T_{\rm eff}$ computed over $T_{\rm eff}^{\rm ref}$ bins of 200 K are shown as red dots and bars, respectively. The mean values of $|\Delta T_{\rm eff}|$ are smaller than 400 K, except for $T_{\rm eff}^{\rm ref} = 5500$ K (500 K) and 4700 K (417 K). The standard deviations of $\Delta T_{\rm eff}$ range between 301 and 912 K, respectively, at $T_{\rm eff}^{\rm ref} = 6300$ and 5500 K. This confirms the dependability of our numerical results for the stellar effective temperatures.

D. Determination of stellar band emissivity

The spectral emissivity in bands 1, 3, and 5 can be obtained by the same token, as illustrated by the corresponding histograms of Figs. 5(a)–5(c). The emissivity of the sampled stars in the three bands shows distinct qualitative behaviors: limited to the narrow range 0.95–1.00 in band 1, centered around 0.90 in band 5, and broadly distributed between 0.90 and 1.00 in band 3.

The emissivity of the sampled stars in bands 1, 3 and 5 have mean, 0.98, 0.92, and 0.95, and standard deviation, 0.0161, 0.0336, and 0.0212, respectively, as displayed in Fig. 5(d). As anticipated, the emissivity data of band 3 are more dispersed. The values of the spectral emissivity illustrated here, combined with the estimates of the effective temperatures reported above, allow a self-consistent calculation of the spectral radiation fluxes from the sampled stars (listed in the supplemental material, Table S1 [61]).

E. Calculation of stellar radiation fluxes in other bands with observational data

So far, data on the stellar radiation fluxes in bands 1, 3, and 5 have been used to train the SPSO algorithm we implemented to solve the inverse problem and thus compute the unknown model parameters. Having determined the model parameters with a satisfactory degree of confidence, we can now solve the direct problem of estimating the radiation fluxes for the same sample of stars, but in bands 2, 4, and 6, and compare our results with the existing

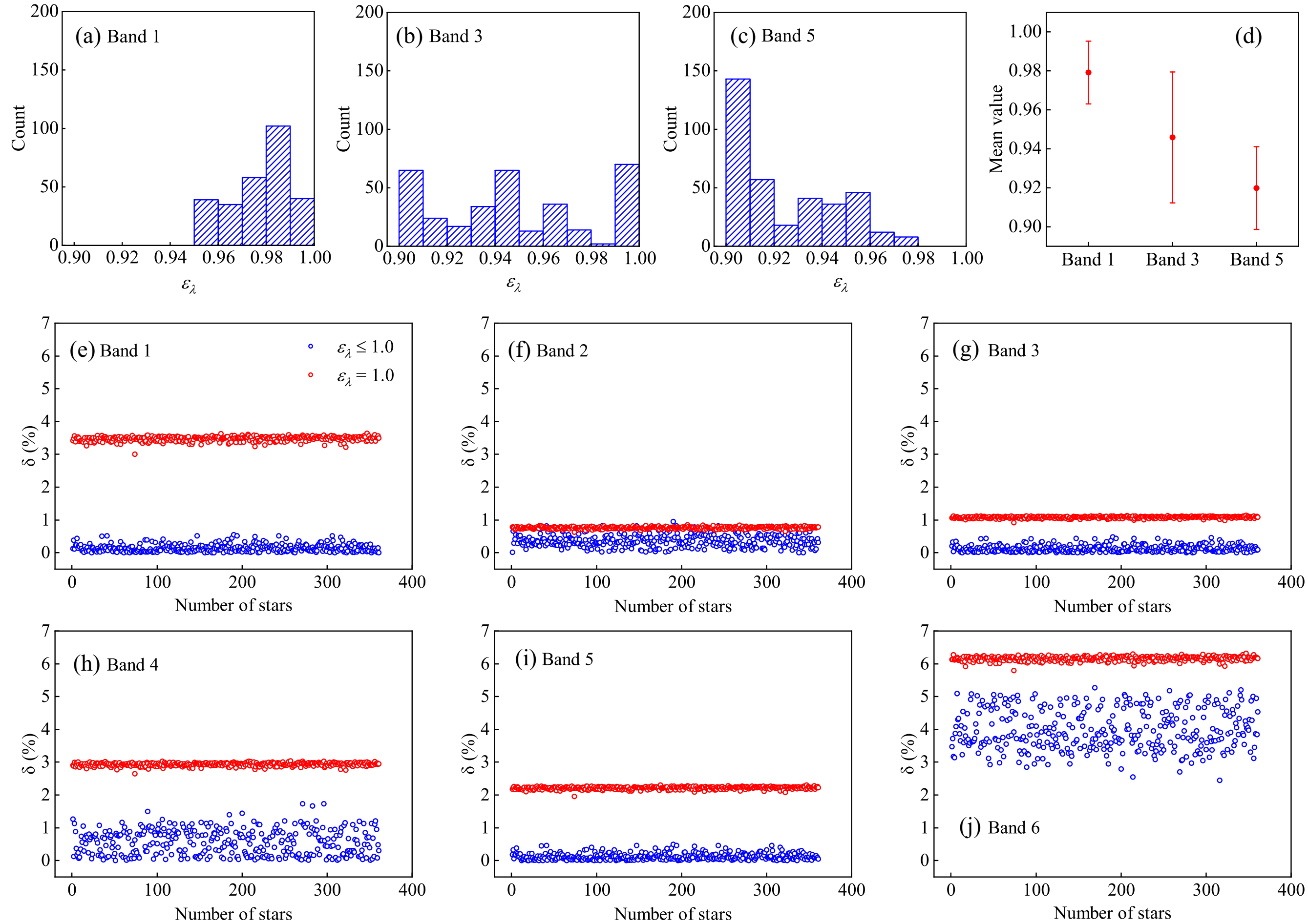

FIG. 5. Emissivity statistics for the sampled stars in (a) band 1, (b) band 3, and (c) band 5 with corresponding mean values and standard deviations shown in (d). Statistics of relative errors of the radiation fluxes δ, Eq. (9), respectively, with emissivity $\varepsilon_\lambda \leq 1.0$ and $\varepsilon_\lambda = 1.0$ in all six bands of the MSX catalog: (e) band 1, (f) band 2, (g) band 3, (h) band 4, (i) band 5, and (j) band 6.

observational data. To this purpose, we approximated the emissivity of band 2 with the emissivity of band 3 and the emissivity of bands 4 and 6 with that of band 5. Our results are detailed in the supplemental material, Table S2. The deviation of our estimates for the radiation fluxes from those reported in the current literature is quantified by the relative error, δ, defined in Eq. (9).

To fully exploit the predictive power of our technique, in Figs. 5(e)–5(j), we compare the relative errors of the radiation fluxes in all bands 1–6 calculated for a larger sample of 361 stars from the MSX catalog, respectively, with emissivity $\varepsilon_\lambda \leq 1.0$ and $\varepsilon_\lambda = 1.0$. Here, $\varepsilon_\lambda = 1.0$ means that the emissivity was set to be 1 during the calculation of the radiation fluxes [44], as customary in the current literature, whereas $\varepsilon_\lambda \leq 1.0$ refers to the use of the actual emissivity value, as obtained self-consistently through our inverse model. It is found that the relative errors of the radiation fluxes with $\varepsilon_\lambda \leq 1.0$ are all smaller than those for $\varepsilon_\lambda = 1.0$, in all six bands. In particular, the relative errors with $\varepsilon_\lambda \leq 1.0$ are smaller than 1% in bands 1, 2, 3, and 5; smaller than 1.74% in band 4; and quite scattered in band 6 with a maximum error of 5.27%. It can be concluded that making use of self-consistent estimates of $\varepsilon_\lambda \leq 1.0$ is a more effective strategy than assuming stars as blackbody sources with $\varepsilon_\lambda = 1.0$.

The results discussed so far are based on data from the MSX catalog covering the infrared range 4.22–25.1 μm. Our conclusions are also corroborated by a preliminary analysis of data from the Large Sky Area Multi-Object Fiber Spectroscopic Telescope (LAMOST) catalog in the optical range 0.37–0.9 μm [40,41]. We choose a sample of 50 stars. The emissivity turns out to be 1.00 in the wavelength range 0.555–0.69 μm (visible light) and 0.90 in the two side ranges, 0.32–0.38 (ultraviolet light) and 0.85–0.97 μm (near-infrared light). See the Appendix for details.

F. Prediction of stellar radiation fluxes in bands without observational data

The spectral emissivity calculated above can also be used to predict the radiation fluxes in spectral bands where observational data are still missing. We did so for the sample of 361 stars taken from the MSX catalog, as shown in the supplemental material, Table S3. For 351 stars, estimates of the effective temperature are reported in the literature, while for the remaining ten stars, no data are currently available. On assuming that the emissivity of the closest known band 3 (4.24–4.45 μm) does not differ much from the emissivity in the unexplored band 4.0–5.0 μm, we computed the radiation fluxes reported in Table S3. Those predictions cannot be compared systematically with existing observational data. The corresponding sparse data reported in the MSX, the Bonner Durchmusterung, and the Henry Draper catalogs are also listed in Table S3 for the sake of a comparison. In general, our estimates range from 0.90 to 1.00 for the emissivity and from 0.22×10^{-13} to 542.0×10^{-13} $\mathrm{W/m^2}$ for the radiation fluxes.

We finally remark that the comparison of the radiation flux data of Table S3 with future direct flux measurements will be straightforward, thanks to the accurate estimates of the corresponding band emissivity provided in the same table. Of course, this technique can be used to fill observational data gaps in any available star catalog.

IV. CONCLUSIONS

We have developed an inverse model to extract stellar band emissivity from astronomical observations. The "emissivity" mentioned in this article is the "effective emissivity," defined as the ratio of the radiation emitted by the stellar surface to the radiation emitted by a standard blackbody at the same temperature. The stellar radiation fluxes in certain spectral bands serve as model input. The stochastic particle swarm optimization algorithm was implemented to optimize the model parameters, namely, spectral emissivity, effective temperature, and detection angular parameter, of the sampled stars. The close agreement between our predictions and the existing observational data is advocated to validate our method. Having optimized our model parameters, we then calculated stellar radiation fluxes in other spectral bands; the relative deviations from the available data are encouragingly small. Making use of self-consistent estimates of the stellar spectral emissivity $\varepsilon_\lambda \leq 1.0$ is a more effective strategy than assuming stars as blackbody sources with $\varepsilon_\lambda = 1.0$. Finally, as a model application, our method predicts the radiation fluxes in spectral bands not populated by telescope observation data and for which only qualitative estimates have been proposed. This work provides an alternative way to estimate stellar emissivity.

ACKNOWLEDGMENTS

We acknowledge financial support from the National Natural Science Foundation of China under Grants No. 11725521 and No. 12035004 and from the Science and Technology Commission of Shanghai Municipality under Grant No. 20JC1414700.

APPENDIX: STELLAR RADIATION FLUXES FROM THE LAMOST STELLAR CATALOG

We apply now our technique to data from the catalog of LAMOST, a telescope located at the Xinglong Observatory in Hebei, China [62]. This catalog provides a spectroscopic survey the wavelength range of 0.37–0.9 μm. The five detected bands, bands 1–5, of the LAMOST catalog are 0.32–0.38, 0.41–0.55, 0.555–0.69, 0.695–0.845, and 0.85–0.97 μm, respectively.

The catalog gives information on the stellar magnitude, information that must be converted into flux density. The relationship between the brightness and magnitude of two celestial bodies is described by Pogson's equation [63],

$$m_2 - m_1 = -2.5 \log \frac{E_2}{E_1}, \tag{A1}$$

where m_1 and m_2 are the stellar magnitudes and E_1 and E_2 are the flux densities. The photometric zero point is usually adopted in applying this formula. The flux density E_1 is the photometric zero point corresponding to the condition $m_1 = 0$. The stellar flux density E_2 can be calculated according to the given stellar magnitude m_2.

Figure 6 shows the relative errors δ of radiation fluxes with emissivity $\varepsilon_\lambda \leq 1.0$ and $\varepsilon_\lambda = 1.0$ for bands 1–5 of the LAMOST catalog. It is found that the relative errors of the radiation fluxes with $\varepsilon_\lambda \leq 1.0$ are smaller than with $\varepsilon_\lambda = 1.0$ in band 1 and band 5. In particular, the relative errors of the radiation fluxes with $\varepsilon_\lambda \leq 1.0$ are less than 8% and 15% for band 1 and band 5, respectively. The relative errors of the radiation fluxes are larger than 140% for band 5 with $\varepsilon_\lambda = 1.0$, which confirms the inadequacy of the assumption $\varepsilon_\lambda = 1.0$. Even though the relative errors of the radiation fluxes with $\varepsilon_\lambda \leq 1.0$ are slightly larger than those with $\varepsilon_\lambda = 1.0$ for band 2, band 3, and band 4, our numerical results are still acceptable. In general, it can be concluded that the model with $\varepsilon_\lambda \leq 1.0$ is more reliable than with $\varepsilon_\lambda = 1.0$.

The stellar radiation fluxes of 50 stars in band 1, band 3, and band 5 are calculated explicitly. The fluxes and emissivity values of the three bands are listed in Table I. OBSID is the unique number identification of this spectrum in the LAMOST catalog. The emissivity of band 3 (visible light) is 1.00. Accordingly, the emissivity values of band 1 (ultraviolet light) and band 5 (near-infrared light) are both 0.90. The temperatures calculated by our model and in the LAMOST catalog are also shown in Table I. The two sets of temperatures are seemingly consistent.

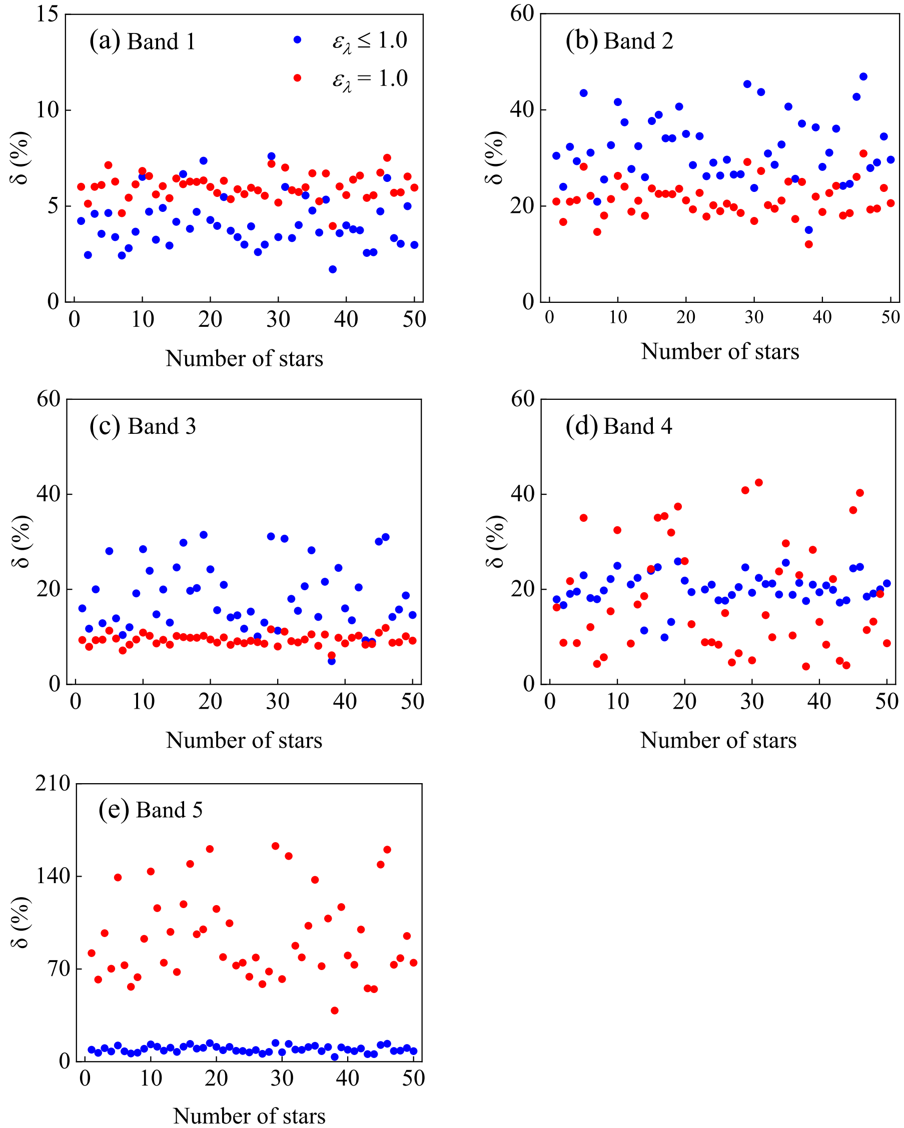

FIG. 6. Statistics of the relative errors δ of the radiation fluxes with emissivity $\varepsilon_\lambda \leq 1.0$ and $\varepsilon_\lambda = 1.0$ in the different bands of the LAMOST catalog: (a) band 1, (b) band 2, (c) band 3, (d) band 4, and (e) band 5.

TABLE I. Calculation of temperatures and stellar radiation fluxes of 50 stars in band 1 (0.32–0.38 μm), band 3 (0.555–0.69 μm), and band 5 (0.85–0.97 μm) of the LAMOST catalog. ε_λ is the emissivity of star at wavelength λ. E_c is the calculated radiation flux (unit: $\times 10^{-19}$ W/m^2).

	OBSID in the LAMOST catalog	Band 1		Band 3		Band 5		Temperature in this work	Temperature in the LAMOST catalog [62]
		ε_λ	E_c	ε_λ	E_c	ε_λ	E_c		
1	101001	0.90	1.177	1.00	5.451	0.90	3.493	5167	5068
2	101005	0.90	1.065	1.00	3.358	0.90	1.843	5873	5529
3	101008	0.90	1.924	1.00	7.857	0.90	4.784	5376	5439
4	101009	0.90	1.330	1.00	4.660	0.90	2.668	5658	5702
5	101016	0.90	1.344	1.00	13.970	0.90	12.469	4144	4647
6	101017	0.90	2.461	1.00	8.228	0.90	4.643	5729	5803
7	101020	0.90	5.903	1.00	13.443	0.90	6.481	6641	6110
8	101021	0.90	7.529	1.00	18.223	0.90	9.000	6478	6059

(Table continued)

TABLE I. *(Continued)*

	OBSID in the LAMOST catalog	Band 1		Band 3		Band 5		Temperature in this work	Temperature in the LAMOST catalog [62]
		ε_λ	E_c	ε_λ	E_c	ε_λ	E_c		
9	101023	0.90	1.571	1.00	5.393	0.90	3.062	5705	5704
10	101024	0.90	0.281	1.00	3.363	0.90	3.184	3996	4139
11	101026	0.90	3.570	1.00	18.097	0.90	12.030	5031	5644
12	101027	0.90	5.735	1.00	16.711	0.90	8.885	6045	5789
13	101028	0.90	3.086	1.00	13.287	0.90	8.266	5287	5709
14	101029	0.90	5.933	1.00	19.754	0.90	11.079	5761	5818
15	101030	0.90	0.595	1.00	5.414	0.90	4.574	4285	4966
16	101032	0.90	0.462	1.00	7.988	0.90	8.804	3678	4344
17	101033	0.90	2.838	1.00	17.905	0.90	13.015	4723	5277
18	101034	0.90	2.425	1.00	15.772	0.90	11.608	4679	5039
19	101035	0.90	0.310	1.00	4.922	0.90	5.236	3746	4381
20	101038	0.90	0.486	1.00	3.562	0.90	2.753	4534	4877
21	101041	0.90	3.611	1.00	14.011	0.90	8.358	5467	5751
22	101042	0.90	2.465	1.00	15.210	0.90	10.954	4746	5271
23	101043	0.90	1.434	1.00	5.627	0.90	3.372	5448	5761
24	101044	0.90	4.777	1.00	16.146	0.90	9.111	5730	5732
25	101048	0.90	1.323	1.00	4.113	0.90	2.244	5900	5537
26	101056	0.90	1.173	1.00	3.597	0.90	1.952	5928	5931
27	101060	0.90	1.202	1.00	2.898	0.90	1.429	6487	6269
28	101061	0.90	2.975	1.00	10.369	0.90	5.924	5671	5572
29	101066	0.90	0.493	1.00	7.912	0.90	8.459	3735	4465
30	101077	0.90	1.211	1.00	3.404	0.90	1.784	6115	6184
31	101079	0.90	0.899	1.00	8.575	0.90	7.385	4230	4808
32	101080	0.90	0.716	1.00	4.227	0.90	2.990	4814	5267
33	101085	0.90	0.708	1.00	2.287	0.90	1.267	5819	5732
34	101092	0.90	1.248	1.00	10.659	0.90	8.774	4346	4719
35	101101	0.90	0.650	1.00	4.327	0.90	3.215	4652	4985
36	101103	0.90	2.993	1.00	10.709	0.90	6.182	5617	5719
37	101106	0.90	1.125	1.00	7.916	0.90	6.016	4577	5125
38	101114	0.90	1.191	1.00	3.180	0.90	1.632	6238	5302
39	101116	0.90	0.501	1.00	11.430	0.90	14.139	3474	4191
40	101120	0.90	0.790	1.00	2.783	0.90	1.596	5649	5601
41	101121	0.90	1.823	1.00	6.388	0.90	3.657	5656	5935
42	101125	0.90	0.788	1.00	4.458	0.90	3.098	4874	5164
43	101136	0.90	1.886	1.00	5.572	0.90	2.979	6008	5407
44	101138	0.90	3.220	1.00	6.659	0.90	3.091	6907	6604
45	101140	0.90	0.531	1.00	9.059	0.90	9.933	3694	4302
46	101144	0.90	1.458	1.00	13.520	0.90	11.510	4258	5026
47	101147	0.90	1.429	1.00	4.464	0.90	2.440	5891	5664
48	101150	0.90	2.895	1.00	11.960	0.90	7.317	5364	5400
49	101154	0.90	1.425	1.00	6.284	0.90	3.948	5246	5442
50	101169	0.90	1.894	1.00	6.849	0.90	3.971	5604	5658

[1] R. R. Coifman, S. Lafon, A. B. Lee, M. Maggioni, B. Nadler, F. Warner, and S. W. Zucker, Nature (London) **563**, 85 (2018).

[2] A. Bédard, P. Bergeron, P. Brassard, and G. Fontaine, Astrophys. J. **901**, 93 (2020).

[3] T. A. Gomez, T. Nagayama, C. J. Fontes, D. P. Kilcrease, S. B. Hansen, M. C. Zammit, D. V. Fursa, A. S. Kadyrov, and I. Bray, Phys. Rev. Lett. **124**, 055003 (2020).

[4] V. Vikram, J. Sakstein, C. Davis, and A. Neil, Phys. Rev. D **97**, 104055 (2018).

[5] M. Clampin, Adv. Space Res. **41**, 1983 (2008).
[6] M. Xiao, K. M. Perez, M. Giannotti, O. Straniero, A. Mirizzi, B. W. Grefenstette, B. M. Roach, and M. Nynka, Phys. Rev. Lett. **126**, 031101 (2021).
[7] G. Pérez-Callejo, E. V. Marley, D. A. Liedahl, L. C. Jarrott, G. E. Kemp, R. F. Heeter, J. A. Emig, M. E. Foord, M. B. Schneider, S. J. Rose, and J. S. Wark, Phys. Rev. Lett. **126**, 085001 (2021).
[8] M. Saillenfest, B. Tabone, and E. Behar, Astron. Astrophys. **617**, A99 (2018).
[9] V. Vikram, J. Sakstein, C. Davis, and A. Neil, Phys. Rev. D **97**, 104055 (2018).
[10] T. Abdelsalhin, A. Maselli, and V. Ferrari, Phys. Rev. D **97**, 084014 (2018).
[11] P.-H. Chavanis, Phys. Rev. D **100**, 083022 (2019).
[12] A. Caputo, H.-T. Janka, G. Raffelt, and E. Vitagliano, Phys. Rev. Lett. **128**, 221103 (2022).
[13] Y. Huang, G. Shi, and K. Zhu, Astrophys. J. **820**, 9 (2016).
[14] X. Xu and Z. Li, Astrophys. J. **856**, 77 (2018).
[15] R. Basu, D. Mitra, and G. I. Melikidze, Astrophys. J. **917**, 48 (2021).
[16] T. Fischer, P. Carenza, B. Fore, M. Giannotti, A. Mirizzi, and S. Reddy, Phys. Rev. D **104**, 103012 (2021).
[17] J. P. Huang, *Theoretical Thermotics: Transformation Thermotics and Extended Theories for Thermal Metamaterials* (Springer, Singapore, 2020), pp. 43–50.
[18] J. Wang, F. B. Yang, L. J. Xu, and J. P. Huang, Phys. Rev. Appl. **14**, 014008 (2020).
[19] S. Yang, J. Wang, G. L. Dai, F. B. Yang, and J. P. Huang, Phys. Rep. **908**, 1 (2021).
[20] L. J. Xu and J. P. Huang, *Transformation Thermotics and Extended Theories: Inside and Outside Metamaterials* (Springer, Singapore, 2023), pp. 177–190.
[21] N. Suzuki and M. Fukugita, Astron. J. **156**, 219 (2018).
[22] E. Rrapaj, A. Sieverding, and Y.-Z. Qian, Phys. Rev. D **100**, 023009 (2019).
[23] T. Li, X. Lin, Y. Yuan, D. Liu, Y. Shuai, and H. Tan, Case Stud. Therm. Eng. **36**, 102215 (2022).
[24] L. J. Xu, G. Q. Xu, J. P. Huang, and C.-W. Qiu, Phys. Rev. Lett. **128**, 145901 (2022).
[25] L. J. Xu, G. Q. Xu, J. X. Li, Y. Li, J. P. Huang, and C.-W. Qiu, Phys. Rev. Lett. **129**, 155901 (2022).
[26] Y. Liang, X. Zhang, J. Cheng, H. Zeng, Y. Fan, and E. Liang, J. Cosmol. Astropart. Phys. 11 (2021) 030.
[27] A. López Ariste, M. Collados, and E. Khomenko, Phys. Rev. Lett. **111**, 081103 (2013).
[28] A. Serenelli, R. D. Rohrmann, and M. Fukugita, Astron. Astrophys. **623**, A177 (2019).
[29] C. Dessert, J. W. Foster, and B. R. Safdi, Phys. Rev. Lett. **125**, 261102 (2020).
[30] E. Weaver, A. Isella, and Y. Boehler, Astrophys. J. **853**, 113 (2018).
[31] M. Malik, E. M. R. Kempton, D. D. B. Koll, M. Mansfield, J. L. Bean, and E. Kite, Astrophys. J. **886**, 142 (2019).
[32] C. Conroy, Annu. Rev. Astron. Astrophys. **51**, 393 (2013).
[33] L. Casagrande, L. Portinari, and C. Flynn, Mon. Not. R. Astron. Soc. **373**, 13 (2006).
[34] T. Nagayama *et al.*, Phys. Rev. Lett. **122**, 235001 (2019).
[35] G. T. van Belle, K. von Braun, D. R. Ciardi, G. Pilyavsky, R. S. Buckingham, A. F. Boden, C. A. Clark, Z. Hartman, G. van Belle, W. Bucknew, and G. Cole, Astrophys. J. **922**, 163 (2021).
[36] C. Megessier, Astron. Astrophys. **289**, 202 (1994).
[37] D. E. Blackwell, M. J. Shallis, and M. J. Selby, Mon. Not. R. Astron. Soc. **188**, 847 (1979).
[38] I. Ramirez and J. Melendez, Astrophys. J. **626**, 446 (2005).
[39] M. A. Fedderke, P. W. Graham, B. Macintosh, and S. Rajendran, Phys. Rev. D **106**, 023002 (2022).
[40] J. Zhong, S. Lépine, J. Hou, S. Shen, H. Yuan, Z. Huo, H. Zhang, M. Xiang, H. Zhang, and X. Liu, Astron. J. **150**, 42 (2015).
[41] M. S. Xiang, X. W. Liu, J. R. Shi, H. B. Yuan, Y. Huang, A. L. Luo, H. W. Zhang, Y. H. Zhao, J. N. Zhang, J. J. Ren, B. Q. Chen, C. Wang, J. Li, Z. Y. Huo, W. Zhang, J. L. Wang, Y. Zhang, Y. H. Hou, and Y. F. Wang, Mon. Not. R. Astron. Soc. **464**, 3657 (2017).
[42] T. Ikeda, V. Cardoso, and M. Zilhão, Phys. Rev. Lett. **127**, 191101 (2021).
[43] C. Zhang, Y. Yuan, Z. Yu, F. Wang, and H. Tan, J. Cosmol. Astropart. Phys. 09 (2018) 026.
[44] C. Zhang, Y. Yuan, H. Zhang, Y. Shuai, and H. Tan, Res. Astron. Astrophys. **16**, 140 (2016).
[45] M. F. Modest, *Radiative Heat Transfer (Third Edition)* (Academic Press, Boston, 2013), pp. 1–30.
[46] K.-W. Suh, Astrophys. J. Suppl. Ser. **256**, 43 (2021).
[47] M. P. Egan and S. D. Price, Astron. J. **112**, 2862 (1996).
[48] J. J. Condon and S. M. Ransom, *Essential Radio Astronomy* (Princeton University Press, Princeton, NJ, 2016), pp. 23–63.
[49] Q. Li, Y. Yang, and Z. Dai, Astrophys. J. **896**, 1 (2020).
[50] F. Y. Wang, Y. Y. Wang, Y.-P. Yang, Y. W. Yu, Z. Y. Zuo, and Z. G. Dai, Astrophys. J. **891**, 1 (2020).
[51] S. A. Tyul'bashev, T. V. Smirnova, E. A. Brylyakova, and M. A. Kitaeva, Mon. Not. R. Astron. Soc. **508**, 2815 (2021).
[52] A. Gallego-Calvente, R. Schödel, A. Alberdi, R. Herrero-Illana, F. Najarro, F. Yusef-Zadeh, H. Dong, J. Sanchez-Bermudez, B. Shahzamanian, F. Nogueras-Lara, and E. Gallego-Cano, Astron. Astrophys. **647**, A110 (2021).
[53] F. Aharonian, R. Yang, and E. de Oña Wilhelmi, Nat. Astron. **3**, 561 (2019).
[54] Y. Yuan, H. Yi, Y. Shuai, F. Wang, and H. Tan, J. Quant. Spectrosc. Radiat. Transfer **111**, 2106 (2010).
[55] L.-Y. Wei, H. Qi, Y.-T. Ren, J.-P. Sun, S. Wen, and L.-M. Ruan, Int. J. Therm. Sci. **124**, 424 (2018).
[56] N. Muttoni, A. Mangiagli, A. Sesana, D. Laghi, W. Del Pozzo, D. Izquierdo-Villalba, and M. Rosati, Phys. Rev. D **105**, 043509 (2022).
[57] K. Jonsell, B. Edvardsson, B. Gustafsson, P. Magain, P. E. Nissen, and M. Asplund, Astron. Astrophys. **440**, 321 (2005).
[58] J. L. Marshall, Astron. J. **134**, 778 (2007).
[59] M. Bergemann and T. Gehren, Astron. Astrophys. **492**, 823 (2008).

[60] C. J. Hansen, F. Primas, H. Hartman, K. L. Kratz, S. Wanajo, B. Leibundgut, K. Farouqi, O. Hallmann, N. Christlieb, and H. Nilsson, Astron. Astrophys. **545**, A31 (2012).

[61] See Supplemental Material at http://link.aps.org/supplemental/10.1103/PhysRevD.106.123035 for the calculation of stellar emissivity in the input bands, radiation fluxes in the other bands with observational data, and predition of radiation fluxes in the absence of observational data.

[62] G. Zhao, Y.-H. Zhao, Y.-Q. Chu, Y.-P. Jing, and L.-C. Deng, Res. Astron. Astrophys. **12**, 723 (2012).

[63] M. Wesołowski, Res. Astron. Astrophys. **22**, 055015 (2022).